Effect of MIL-53 (Al) MOF particles on the chain mobility and crystallization of poly(L-lactic acid)

Kathuria, Ajay; Brouwers, Niels; BUNTINX, Mieke; Harding, Trevor & Auras, Rafael (2017) Effect of MIL-53 (Al) MOF particles on the chain mobility and crystallization of poly(L-lactic acid). In: JOURNAL OF APPLIED POLYMER SCIENCE, 134, p. 1-8 (Art N° 45690).

DOI: 10.1002/APP.45690
Handle: http://hdl.handle.net/1942/24427

Effect of MIL-53 (Al) MOF particles on the chain mobility and crystallization of Poly(L-lactic acid)

Ajay Kathuria[1*], Niels Brouwers[1, 2], Mieke Buntinx[2], Trevor Harding[3], Rafael Auras[4]

[1] Industrial Technology and Packaging, California Polytechnic State University, San Luis Obispo, CA 93407, USA

[2] Packaging Technology Center, IMO-IMOMEC, Hasselt University, 3590 Diepenbeek, Belgium

[3] Materials Engineering, California Polytechnic State University, San Luis Obispo, CA 93407, USA

[4] School of Packaging, Michigan State University, East Lansing, MI, USA 48824-1223

[*] Corresponding author:

P: (805) 756-2944; F: (805) 756-6111; E: akathuri@calpoly.edu

Accepted manuscript Journal of Applied Polymer Science

Abstract

Polymer-filler interactions significantly influence morphology, functionality and various desirable properties of mixed matrix membranes (MMMs). In this study, chain mobility and crystallization of Poly(L-lactic acid) (PLLA) MMM films prepared by solvent casting PLLA with 1, 5, 10 and 20% wt./wt. of MIL-53(Al) metal organic framework (MOF) were evaluated. The fabricated MMMs were characterized using Differential Scanning Calorimetry (DSC), Fourier Transform Infrared Spectroscopy (FTIR), Thermogravimetric Analysis (TGA), and Scanning Electron Microscopy (SEM). DSC studies indicated that the addition of MOF particles in the PLLA matrix reduces the polymeric chain mobility, which affects the crystallization process. The percent crystallinity of neat PLLA was found to decrease from 4% in neat PLLA to completely amorphous structures in PLLA-10% and PLLA-20% MMMs, as observed in the second heating cycle. FTIR data supports these observations. TGA results showed that PLLA-MOF films are thermally less stable than neat PLLA suggesting that MOF particles act as a depolymerization catalyst for PLLA. Partial agglomeration of MOF particles was observed in the samples using SEM studies. This study indicates strong PLLA-MIL-53(Al) MOF interactions. In addition, this study also provides insight into the effect of MOF particles on the segmental mobility and morphology of PLLA-MIL-53 (Al) composite films.

1. Introduction

Fillers, functional materials, additives or modifiers have been widely used to improve the functionality of polymeric matrices, including strength, stiffness, hardness, durability, permeability and controlled selective exchange of gases for various applications [1-3]. Interfacial interactions between the matrix and filler play an influential role in polymer-filler dynamics. Surface area, concentration and particle size of the filler influence the polymeric chain structure, segmental mobility and crystallinity [4-5]. The interfacial region and its surroundings behave differently from the bulk polymeric matrix. Good polymer-filler interactions can create topological restraints, which may hinder the mobility of polymeric chains. On the other hand, poor interfacial interactions lead to interfacial voids or defects [1, 3, 5-8].

Poly(lactic acid) (PLA) is a bio-based, bio-degradable and compostable polymer that has consolidated its market presence due to techno-commercial advancement, growing production capacity and economic viability [9-10]. PLA is a clear, rigid thermoplastic with mechanical strength comparable to poly(ethylene terephthalate) (PET) and polystyrene (PS). However, various inherent limitations such as its brittle nature, poor barrier performance and slow crystallization kinetics limit its wide scale commercial use [1].

Metal-organic frameworks (MOFs) belongs to a class of microporous, high surface area crystalline materials synthesized by coordinating metal ions with organic struts [11]. Their varied synthesis techniques and potential application in areas such as catalysis, gas storage, gas separation, selectivity, chemical sensing, encapsulation and drug delivery have been comprehensively reported by researchers in the last two decades [11-14]. These

58 reticulate symmetrical crystals can be designed with specific structural properties to meet
59 desired objectives among other organic, inorganic and hybrid porous structures [15-17].

60 MIL-53 (Al) is a highly flexible, thermally and structurally stable, hydrolysis
61 resistant commercially available microporous MOF which is formed by coordination of
62 trivalent aluminum with benzene dicarboxylate struts. It is known for its high surface area,
63 high CO_2 adsorption and selectivity [18, 19]. Ferey *et al.* [20] reported that MIL-53 (Al)
64 has high sorption and selectivity for CO_2 gas over other gases such as O_2 and CH_4. In
65 addition, MIL-53 (Al) is known for its distinct breathing attribute due to the reversible pore
66 expansion and contraction behavior under varying sorbent pressure [21].

67 Ease of processibility and cost effectiveness of the polymers along with high
68 selectivity of MOF particles motivates fabrication of polymer-MOF mixed matrix
69 membranes (MMMs). The polymer-MOF interfacial interaction, polymeric chain mobility,
70 crystallization kinetics and percentage crystallinity of a polymer significantly influences
71 its performance and functionality. Traditionally, interfacial studies have attracted attention
72 in order to achieve higher stress transfer for superior mechanical performance.
73 Additionally, poor interfacial adhesion, or the presence of defects, affects various
74 important properties including gas diffusion and permeability. In the case of polymer-MOF
75 composites, five types of interfacial morphologies have been reported depending on the
76 interfacial interactions are: a). two phase defect free, b). poor interactions leading to voids
77 c). dilated d). increased density e). plugged morphology which can significantly impact
78 their transmission, permeability and perm-selectivity [22]. Such selectively permeable
79 polymer-membranes system can be tailored to gas composition in the headspace of a

product-package system to optimize the shelf life of various consumer products including respiring product such as fresh produce, cheese etc.

Chain mobility is of great significance during the final stages of polymer processing. In addition, segmental chain mobility can influence the physical aging of polymeric materials, which can alter functional properties particularly in glassy polymers including permeability and selectivity [23-24]. Poly (L-lactic acid) (PLLA), a low entanglement density polymer, has demonstrated further decrease in the entanglement density with physical aging due to segmental mobility of the chains [23]. Such microstructural changes can adversely affect various functional properties including mechanical performance, gas transportation and transparency. Previous studies have linked reduced segmental mobility of polymer-nanocomposites with strong interfacial interactions [1, 24-25]. Segmental mobility of PLA chains is of profound interest as it influences crystallinity, as well as its mechanical, barrier and other functional properties [7-8, 26].The purpose of this study was to evaluate the effect of MIL-53 (Al) MOF particles on the segmental mobility and crystallization of solvent cast PLLA films. The effect of varying MOFs fraction on the PLLA matrix was analyzed by using an array of characterization techniques.

2. Methodology

2.1 Materials

Poly(L-lactic acid) (PLLA) resin grade 4043 D, (98% L-lactide) pellets were supplied by NatureWorks LLC (Blair, NE, USA). The weight average molecular weight (M_w) was 111 kDa, with a number average molecular weight (M_n) of 84 kDa and a polydispersity index

(M_w/M_n) of 1.3. MIL-53 (Al) MOF produced by BASF® was acquired from Sigma-Aldrich (St. Louis, MO, USA) under the trade name of Basolite™ A100 MOF ($C_8H_5AlO_5$), with a surface area between 1,100 and 1,500 m^2g^{-1} and particle size distribution of 31.55 μm. Chloroform [anhydrous ≥99%] was purchased from Sigma-Aldrich, St. Louis, MO, USA.

2.2 Methods

PLLA pellets were dried at 80 °C for 4 h using a Thermo Fisher Scientific VWR Oven (Fisher Scientific, Waltham, MA, USA) with a negative pressure of 2.93 kPa and packed in an air tight glass bottle. Three grams of dried PLLA pellets were gradually poured into 75 mL of chloroform at 23 °C while mixing the solution with a magnetic stir plate (Fisher Scientific, Waltham, MA, USA) at 300 RPM for approximately 90 min until all PLLA pellets were dissolved. Basolite™ A100 MOF ($C_8H_5AlO_5$) particles were crushed by applying light, concentric pressure using a Green Marble Mortar & Pestle. PLLA, PLLA-1% MOF, PLLA-5% MOF, PLLA-10% MOF and PLLA-20% MOF were processed by solvent casting. The desired MOF content was weighed using a Mettler Toledo Scale, Model ME54E (Columbus, OH, USA) and poured in the dissolved PLLA-chloroform solution while mixing the solution with the magnetic stir plate rotating at 300 RPM for 10 s. Ultrasonication was performed on the PLLA-MOF-chloroform solution using a Q500 ultrasonicator purchased from QSonica, LLC (Newtown, CT, USA). An on-off cycle was programmed to ultrasonicate for 3 min, with an on cycle time of 3 s at a frequency of 20 kHz and an alternating off cycle of 0 Hz for 2 s. The ultrasonicated solution was poured into teflon coated molds and covered with two layers of holed Al foil to control the chloroform evaporation rate. After completely evaporating the chloroform, the solid samples were placed in the vacuum oven at 23 °C and a negative pressure of 22 mmHg to

extract the residual chloroform from the samples. Samples were stored in vacuum bags at room temperature until the beginning of the different tests. The resulting films had an average thickness of 178 ± 25 μm (7.00 ± 1.0 mil).

2.3 Differential Scanning Calorimetry (DSC)

DSC analysis of neat PLLA and PLLA-MIL 53 (Al) MMM films was performed using a DSC Q1000 (TA instruments, DE, USA). Samples size between 5 and 10 mg were obtained from the films and non-hermetically sealed in an aluminum pan and placed with the reference pan in the DSC cell and run in triplicates. Heat/cool/heat cycles from 0 °C to 180 °C at a rate of 10 °C min $^{-1}$ were performed under a constant nitrogen flow of 50 mL/min. To disregard the thermal history during processing or storage, the second heating cycle was used to determine the glass transition temperature (T_g), cold crystallization onset (T_{co}), melting temperature (T_m) and to calculate the enthalpy of cold crystallization (ΔH_c) and fusion (ΔH_m). The percent crystallinity *Xc* (%) was estimated using the following equation:

$$X_c(\%) = \frac{\Delta H_m - \Delta H_c}{\Delta H_m^c (1-x)} \times 100$$

where ΔH_m is enthalpy of fusion; ΔH_c is the enthalpy of cold crystallization; ΔH^c_m is enthalpy of fusion of pure crystalline PLA (ΔH^c_m = 93.1 J/g [27]) and *x* represents the mass fraction of the MOF in the films. Universal Analysis software version 2000 (TA Instruments, DE, USA) was used to analyze the data. Samples were run in triplicates.

2.4 Fourier Transform Infrared Spectroscopy (FTIR)

Fourier Transform Infrared Spectroscopy (FTIR) of MIL 53 (Al) MOF, cast PLLA and PLLA-MIL-53 (Al) MMM films was performed using an attenuated total reflectance

147 (ATR) module attached to FTIR model IRaffiny-1S (Shimadzu, CA, USA). The spectra
148 were acquired in absorption mode at room temperature in the range of 4000-400 cm^{-1} at 2
149 cm^{-1} resolution using 40 accumulated scans. The background spectra used for reduction
150 were collected at room temperature and samples were examined in triplicates.

151 ***2.5 Thermogravimetric Analysis (TGA)***

152 Thermogravimetric analyses of MIL-53 Al-MOF, neat PLLA and PLLA-MOF films were
153 investigated using a TGA Q50 (TA instruments, DE, USA) under sample nitrogen flow of
154 60 mL min^{-1} and balance purge flow of 40 mL min^{-1}. Samples between 5 and 10 mg were
155 obtained from the films and were placed in an aluminum pan before being heated at a rate
156 of 10 °C min^{-1} from room temperature to 600 °C. Universal Analysis software version 2000
157 (TA Instruments) was used to analyze the data and samples were run in triplicates.

158 ***2.6 Scanning Electron Microscopy (SEM)***

159 Morphological analysis was performed using a Philips Quanta 200 Environmental
160 Scanning Electron Microscope (FEI, Hillsboro, OR, USA) in low vacuum mode (100 Pa)
161 with the use of a tungsten filament. SEM micrographs of the MOF powder, surfaces of
162 solvent cast PLLA and PLLA-MIL-53 (Al) MMM films were obtained at an accelerating
163 voltage of 12.5 kV.

164 ***2.6 Oxygen Gas Permeability Coefficient***

165 The oxygen transmission rates of the PLLA and PLLA-20% MOF were measured as per
166 ASTM D3985-05 using an Oxtran® 2/21 (MOCON Inc., Minneapolis, MN, USA) at 23 °C
167 and 0% RH using 100% oxygen gas as permeant and 98 % N_2/ 2% H_2 as the carrier gas at
168 a flow rate of 20 sccm of the test gas and 10 sccm flow rate of carrier gas. The data was
169 collected every 30 min. until stable saturated state was achieved. The transmission rate of

4-6 mil thick films was measured using aluminum masks with 3.14 cm^2 area. The average value of the last ten stable points was used to calculate the permeability values. The data were analyzed for at least three samples.

2.7 Data Analysis

Data analysis was carried out using SAS 9.4 Software (SAS Institute Inc., Cary, NC, USA). Analysis of Variance (ANOVA) was evaluated using Tukey's HSD (Honestly Significant Differences) at 95% confidence interval ($\alpha = 0.05$).

3. Results and discussion

3.1 Differential Scanning Calorimetry

DSC thermograms of PLLA and PLLA-MIL-53(Al) MMMs are represented in Figure 1. The onset of cold crystallization in PLLA and PLLA-1% MOF was observed at 105.1 and 108.6 ^oC, respectively. A shift in the onset of cold crystallization temperature of the PLLA-1% MOF composition can be attributed to the good interactions between the polymeric chains and the MOF crystals and high surface area of MOF hindering the segmental mobility of the polymeric chains [1, 3, 28]. Such topological constraint can affect crystallization kinetics and viscoelastic properties of the materials. Gagliradi *et al.* [28] studied the interfacial interaction of poly(dimethylsiloxane) with 20 and 40% silica nanoparticles and poly(vinyl acetate) with 40% silica nanoparticles. They observed decreased segmental mobility, which was linked to the specific surface area (SSA) of the nanoparticles, altered chain structure and changed behavior near the interfacial region compared to the bulk polymeric region [28]. The extent of chain restriction also sequentially increased with increase in silica nanoparticle SSA and loading in the polymeric matrix. In another study, Fragiadakis *et al.* [29] reported higher relaxation time

193 in the interfacial region for uniformly distributed natural rubber nano-silica particle based
194 composite systems. In this work, the absence of cold crystallization at higher MOF weight
195 fraction can be ascribed to the fact that more polymeric volume fraction was restricted due
196 to the presence of these particles.

197 **<Figure 1>**

198 Detailed analysis of the DSC thermograms of PLLA and its composites is provided
199 in Table 1. The increase in the T_g with increase in the MOF loading further indicates
200 reduced segmental mobility. We obtained highly amorphous neat solvent cast PLLA
201 samples with 3.2% crystallinity. The crystallinity further decreased from 3.1 to 0.5% with
202 1 and 5% MOF loading in these composites. PLLA-10% MOF and PLLA-20% MOF were
203 completely amorphous. At these higher MOF loadings, the cold crystallization peaks were
204 absent in the second heating cycle due to reduced chain mobility which could be ascribed
205 to strong polymer-filler interactions. The decreased percentage crystallinity with increase
206 in the MOF content can be correlated to the decreased mobility of the polymeric chains
207 [3]. Although, change in the percentage crystallinity appear to be relatively smaller
208 primarily due to amorphous nature of the polymer. The enthalpy of cold crystallization
209 represented in Table 1 provides a better picture of chain mobility. The enthalpy of chain
210 mobility of PLLA decreased from 8.7 $J.g^{-1}$ to 2.7 $J.g^{-1}$ with the addition of the 1% MIL-53
211 (Al) MOF. We did not observed any cold crystallization peaks at higher MOF loadings.

212 **< Table 1>**

213

3.2 Thermogravimetric Analysis (TGA)

Figure 2a and 2b show TGA thermograms and derivative profiles for MOF, neat PLLA and PLLA-MOF films. The first significant weight loss peak observed between 130-140 °C can be ascribed to the small weight loss (2-3%) of volatile compounds such as chloroform used for solvent casting or water molecules entrapped in the plastic. Data obtained from TGA thermograms is presented in Table 2. Degradation peaks were not observed in MOF below 500ºC due to its high thermal stability [30]. The onset of thermal degradation of PLLA, PLLA-1% MOF, PLLA-5% MOF, PLLA-10% MOF and PLLA-20% MOF was observed at 341.6, 330.9, 321.6, 319.6 and 315.2 ºC, respectively. The sharp weight loss observed between 300-376 °C can be ascribed to the thermal degradation of the polymeric chains. Degradation peaks as obtained from derivative profile were observed at 376.6, 359.3, 354.1, 351.2 and 354.5 ºC for PLLA, PLLA-1% MOF, PLLA-5% MOF, PLLA-10% MOF and PLLA-20% MOF, respectively. It was also observed that PLLA-MOF composites weight loss peaked around 2.5 %.°C^{-1} whereas PLLA degradation peaked to 2.35 %.°C^{-1}. The decrease in the onset of thermal degradation temperature, decrease in the degradation peak temperature and increase in the weight loss rate as observed in the first derivative profile (Figure 2b) with the addition of MOF samples can be associated with the MOF particles acting as depoylmerization catalysts, which reduced the thermal degradation activation energy [31-33]. Transition metal based complex compounds including MOF particles have been widely recognised for their catalytic activity due to their partial filled d-orbitals or unsaturated metal sites [34]. Fan *et al.* [32] studied thermal degradation of PLLA in the presence of either 5 wt% calcium oxide (CaO) or 5 wt% magnesium oxide (MgO). Based on the differential thermogravimetric profiles,

they observed that onset of thermal degradation of PLLA dropped from 270 to 180 and 210ºC for PLLA-5% CaO and PLLA-5% MgO systems, respectively. Dai *et al* [35] fabricated PLA composites with Zn (II) - pyridine 2,5 dicarboxylate MOF. They also observed decreased thermal stability of PLA at elevated tempeartures, which was ascribed to unzipping depolymerization. On the other hand, the degradation of PLA has been reported to be a complex phenomenon due to random scissions leading to linear and cyclic oligomers, which can potentially recombine leading to complex byproducts [35, 36].

< Figure 2a and 2b, Table 2>

3.3 Fourier Transform infrared spectroscopy (FTIR)

To understand the effect of MOF on the PLLA polymeric matrix, PLLA and MOF peaks were superimposed, and peaks which exist only in PLLA matrix were discriminated for further analysis. Figure 3a provides the FTIR spectra of PLLA and PLLA-MIL-53 (Al) MMMs. The FTIR peaks between 2850 and 3000 cm^{-1} have been assigned to the symmetric and asymmetric stretch of methyl and methylene groups. Medium intensity asymmetric -CH_3 vibration (stretching) and symmetric -CH_3 vibration (stretching) have been observed at 2977 and 2952 cm^{-1}. Various factors can significantly impact peak intensity strength of these bands depending on the structure, chain architecture, and packing [37-40]. In addition, orientation, crystallinity and chain restriction can also affect the intensity of various vibrational peaks [41]. We observed a significant decrease in the peak intensity of -CH_3 (asymmetric and symmetric), carbonyl, and C-O-C group vibrations with addition of 1 wt. % MOF particles in the PLLA matrix compared to that of the neat PLLA. This decrease can be related to decreased crystallinity and hindered mobility of the PLLA chains due to the strong favorable interfacial interactions between PLLA and MOF particles [1,

42-43]. Yu *et al* [42] reported decreased FTIR peak intensity for poly(vinylidene fluoride) in 2850 to 3000 cm^{-1} wavenumber region with the addition of nanoclay. The decreased intensity was ascribed to the strong interaction between polymer and clay platelets which impeded the chain mobility resulting in reduced infrared absorption in this region. The systematically amplified intensity decrease with the increase in the nano-clay content from 0.2 to 10 wt% clay also supports the DSC observations.

<Figure 3a>

Figure 3b shows FTIR spectra around 1750 cm^{-1} band generally correlated with *v*(C=O) interchain dipole-dipole interaction. These interchain dipole-dipole interactions depend on the distance between the chains and are influential when the distance between the C=O neighboring molecules is less than 2.7 Å [43]. Reduced peak intensity indicates reduced interactions which is supported by the decrease in the crystallinity.

<Figure 3b>

FTIR spectra ranging from wavenumbers 100-800 cm^{-1} are presented in Figure 3c. Wavenumber 871 cm^{-1} has been associated to 10_3 helix conformation which has been linked with the alpha crystals in the PLA [37]. The decreased intensity around this wavenumber is also indicative of the reduced crystallinity due to reduced mobility of PLA chains.

<Figure 3c>

3.4 Scanning Electron Microscopy (SEM)

Figure 4 a-f show SEM images of MOF particles, PLLA and various compositions of PLLA-MIL-53 (Al) MMMs. Poor polymer MOF interactions can result in non-selective

interfacial voids. Therefore, a defect free morphology with strong interfacial interaction between filler and polymeric matrix is a precondition to obtaining superior functional performance of these membranes. We observed defect free polymer-filler morphology for PLLA-MIL-53 (Al) MMMs in Figure 4 c to f, which supports our finding of strong interactions between PLLA and MIL-53 (Al) MOF as also supported by DSC and FTIR studies.

<Figure 4 a-f>

3.5 Oxygen Permeability

Various industrial or consumer applications such as fresh produce packaging may desire selective and tailored oxygen gas permeability. Controlled oxygen gas permeability may help in extending the shelf life of respiring produce. For oxygen mass transfer 20 wt% MIL-53 (Al) was carefully chosen based on the previous research works its quadrupole moment and polarizability [3, 19, 44-45]. Table 3 shows O_2 permeability coefficients of PLLA and PLLA-20% MIL-53 (Al) MOF. Oxygen permeability coefficient increased by 26% with the addition of 20% Mil-53 (Al) MOF. Improved oxygen gas breathability of these composites can be ascribed to the strong interactions between organic linkers and oxygen gas molecules [19].

4. Conclusions and Future Work

In this study, PLLA, PLLA- 1% MIL-53(Al), PLLA- 5% MIL-53(Al), PLLA- 10% MIL-53(Al) and PLLA- 20% MIL-53(Al) MMM films were fabricated using a solvent casting process. DSC, FTIR and SEM data supported good interfacial interactions between PLLA and MIL-53(Al) MOF. Favorable polymer-filler interactions reduced segmental mobility of the chain affecting the crystallinity. Completely amorphous PLLA-MIL-53(Al) MMM films were obtained at 5 wt.% MOF or above. The presence of MOF increased the rate of degradation of PLLA by de-polymerization reaction as observed in TGA studies. These membranes can easily be fabricated on mass scale by using master-batch and using cast film extrusion provided favorable economics. The future studies can explore the commercialization of these membrane systems.

Acknowledgments

The authors would like to thank funding from Cal Poly State University and Orfalea Mini Summer Support Research Grant. Authors would also like to thank Eric Futak, Jeffrey Norton, Jessie O'Connell, and Nestor Vazquez for help with the experiments. Authors also thank University of Hasselt for allowing Niels Brouwers to study abroad for his graduate research work. Authors are also thankful to IAPRI for awarding Niels Brouwers a scholarship to travel to Cal Poly.

References

1. Kathuria A, Abiad MG, and Auras R. Toughening of poly(L-lactic acid) with Cu_3BTC_2 metal organic framework crystals. Polymer 2013; 54: 6979-6986.
2. Kathuria A, Al-Ghamdi S, Abiad MG, and Auras R. The influence of $Cu_3(BTC)_2$ metal organic framework on the permeability and perm-selectivity of PLLA-MOF mixed matrix membranes. Journal of Applied Polymer Science 2015; 42764 (1-10).
3. Kathuria A, Abiad MG, and Auras R. Deterioration of metal-organic framework crystal structure during fabrication of poly(L-lactic acid) mixed-matrix membranes. Polymer International 2013; 62: 1144-1151.
4. Saiter A, Delpouve N, Dargent E, Oberhauser W, Conzatti L, Cicogna F, Passaglia E. Probing the chain segment mobility at the interface of semi-crystalline polylactide/clay nanocomposites. European Polymer Journal 2016; 274-289.
5. Jiang N, Endoh MK, Koga T, Masui T, Kishimoto H, Nagao M, Satija SK, Taniguchi T. Nanostructures and Dynamics of Macromolecules Bound to Attractive Filler Surfaces. ACS Macro Letters 2015; 4: 838-842.
6. Robertson CG, Lin CJ, Rackaitis M, and Roland CM. Influence of particle size and polymer-filler coupling on viscoelastic glass transition of particle-reinforced polymers. Macromolecules 2008; 41: 2727-2731.
7. Cho SY, Park HH, Yun YS, and Jin H-J. Influence of Cellulose nanofibers on the morphology and physical properties of poly(lactic acid) foaming by supercritical carbon dioxide. Macromolecular Research 2013; 21: 529-533.
8. Mofokeng JP, Luyt AS, Tabi T, and Kovacs J. Comparison of injection moulded natural fibre-reinforced composites with PP and PLA as matrices. Journal of Thermoplastic Composite Material 2011, 25: 927-948.
9. Castro-Aguirre E, Iniguez-Franco F, Samsudin H, Fang X, and Auras R. Poly(lactic acid)-Mass production, processing, industrial applications, and end of life. Advanced Drug Delivery Reviews 2016; 107: 333-366.
10. Saeiddlou S, Huneault MA, Li H, and Park CB. Poly(lactic acid) crystallization. Progress in Polymer Science 2012; 37: 1657-1677. Nature 1999; 402: 276-279.
11. Li H, Eddaoudi M, O'Keeffe M, and Yaghi OM. Design and synthesis of an exceptionally stable and highly porous metal-organic framework.
12. Rastogi S, Yao Y, Lippits DR, Höhne GWH, Graf R, Spiess HW, Lemstra PJ. Segmental mobility in the non-crystalline regions of semicrystalline polymers and its implications on melting. Macromolecular Rapid Communication 2009; 30: 826-839.
13. Al-Ghamdi S, Kathuria A, Abiad M and Auras R. Synthesis of nanoporous carbohydrate metal-organic framework and encapsulation of acetaldehyde. Journal of Crystal Growth 2016; 451: 72-78.
14. Lee JY, Farha OK, Roberts J, Scheidt KA, Nguyen ST, and Hupp JT. Metal-organic framework materials as Catalyst. Chemical Society Reviews 2009; 38: 1450-1459.
15. Kreno LE, Leong K, Farha OK, Allendorf M, Duyne RPV, and Hupp JT. Metal-Organic Framework Materials as Chemical Sensors. Chemical Reviews 2012;

16. Porous metal-organic framework nanoscale carriers as a potential platform for drug delivery and imaging. Nature Materials 2010; 9: 172-178.

17. James SL. Metal-organic frameworks. Chemical Society Reviews 2003; 32: 276-288.

18. Mihaylov M, Chakarova K, Andonova S, Drenchev N, Ivanova E, Pidko EA, Sabetghadam A, Seoane B, Gascon J, Kapteijn F, and Hadjiivanov K. Adsorption of CO_2 on MIL-53 (Al): FTIR evidence of the formation of dimeric CO_2 species. Chemical Communications 2016; 52: 1494-1497.

19. Rallapalli P, Prasanth KP, Patil D, Somani RS, Jasra RV, Bajaj HC. Sorption studies of CO_2, CH_4, N_2, CO, O_2 and Ar on nanoporous aluminum terephthalate [MIL-53(Al)]. Journal of Porous Materials 2011; 18: 205-210.

20. Férey G, Latroche M, Serre C, Millange F, Loiseau T and Percheron-Guégan A. Hydrogen adsorption in the nano-porous metal benzenedicarboxylate M(OH)(O2C–C6H4–CO2) (M = Al3+, Cr3+), MIL-53. Chemical Communications 2003; 2976-2977.

21. Bourrelly S, Llewellyn PL, Serre C, Millange F, Loiseau T, and Férey G. Different Adsorption Behaviors of Methane and Carbon Dioxide in the Isotypic Nanoporous Metal Terephthalates MIL-53 and MIL-47

22. Vinh-Thang H, and Kaliaguine S. Predictive models for mixed-matrix membrane performance: A review; Chemical Review 2013; 113:4980-5028.

23. Pan P Zhu B and Inoue Y. Ethalpy relaxation and embrittlement of poly(L-lactide) during physical aging. Macromolecules 2007; 40: 9664-9671.

24. Cangialosi D, Boucher VM, Alegria A, and Colmenero J. Physical aging in polymers and polymer nanocomposites: recent results and open questions. Soft Matter 2013; 9: 8619-8630.

25. Napolitano S, and Wubbenhorst M. The life time of the deviations from bulk behavior in polymers confined at the nanoscale. Nature Communications 2011; 2: 260.

26. Huang HD, Ren PG, Xu JZ, Xu L, Zhong GJ, Hsiao BS, and Li ZM. Improved barrier properties of poly(lactic acid) with randomly dispersed graphene oxide nanosheets. Journal of Membrane Science 2014; 464: 110-118.

27. Dorgan J R, Rheology of Poly(lactic acid). Poly(Lactic Acid): Synthesis, Structures, Properties, Processing, and Applications, Edited by Auras R, Lim L, Selke S and Tsuji H, Wiley Series Published 2010; Chapter 10: 125-139.

28. Gagliradi S, Arrighia V, Ferguson R and Telling MTF. Restricted dynamics in polymer-filler systems. Physica B 2001; 301: 110–114.

29. Fragiadakis D, Bokobza L, and Pissis P. Dynamics near the filler surface in natural rubber-silica nanocomposites. Polymer 2011; 52: 3175-3182.

30. Loiseau T, Serre C, Huguenard C, Fink G, Taulelle F, Henry M, and bat A rationale for the large breathing of the porous Aluminum Terephthalate (MIL-53) upon hydration.

31. Motoyama T, Tsukegi T, Shirai Y, Nishida H, and Endo T. Effects of MgO catalyst on depolymerization of poly-L-lactic acid to L,L-lactide. Polymer degradation and stability 2007; 92: 1350-1358.

32. Fan Y, Nishida H, Mori T, Shirai Y, and Endo T. Thermal degradation of poly(L-lactide): effect of alkali earth metal oxides for selective L, L-lactide formation. Polymer 2004; 45: 1197-1205.

399 33. Tsuji H and Fukui I. Enhanced thermal stability of poly(lactide)s in the mely by enantiomeric
400 polymer blending. Polymer 2003; 10: 2891-2896.

401 34. Yoon JW, Seo Y-K, Hwang YK, Chang J-S, Leclerc H, Wuttke S, Bazin P, Vimont A, Daturi
402 M, Bloch E, Llewellyn PL, Serre C, Horcajada P, Greneche J-M, Rodrigues AE, Ferey G.
403 Controlled Reducibility of a Metal-Organic Framework with Coordinatively unsaturated sites
404 for preferential gas sorption. Angewandte Chemie 2010; 122: 6085-6088.

405 35. Dai X, Cao Y, Shi X, and Wang X. Non-isothermal crystallization kinetics, thermal degradation
406 behavior and mechanical properties of poly(lactic acid)/MOF composites prepared by melt-
407 blending methods. RSC Advances 2016; 2046-2069.

408 36. Yu H, Huang N, Wang C and Tang Z. Modeling of poly(L-lactide) thermal degradation:
409 theoretical prediction of molecular weight and polydispersity index. Journal of Applied
410 Polymer Science 2003; 88: 2557–2562.

411 37. Poly(Lactic Acid): Synthesis, Structures, Properties, Processing, and Applications, Edited by
412 Auras R, Lim L, Selke S and Tsuji H, Wiley Series Published 2010; Chapter 8: 97-112.

413 38. Robinson JW, Frame EMS, Frame II GM. Undergraduate Instrumental Analysis, Sixth Edition,
414 MARCEL DEKKER, NY.

415 39. Verma SP, Wallach DFH. Raman spectra of some saturated, unsaturated and deuterated C_{18}
416 fatty acids in the HCH-deformation and CH-stretching regions.

417 40. Messmer MC, Conboy JC, and Richmond GL. Observation of molecular ordering at the liquid-
418 liquid interface by resonant sum frequency generation. Journal of the American Chemical
419 Society 1995; 17: 8039-8040.

420 41. Paragkumar NT, Edith D and Six JL. Surface characteristics of PLA and PLGA films. Applied
421 Surface Science 253: 5; 2758-2764.

422 42. Yu L and Cebe P. Crystal polymorphism in electrospun composite nanofibers of
423 poly(vinylidene fluoride) with nanoclay. Polymer 2009; 50: 2133-2141.

424 43. Zhang J, Tsuji H, Noda I, and Ozaki Y. Structural changes and crystallization dynamics of
425 Poly(L-lactide) during the cold-crystallization process investigated by infrared and two-
426 dimensional infra-red correlation spectroscopy. Macromolecules 2004; 37: 6433-6439.

427 44. Adams R, Carson C, Ward J, Tannenbaum R, Koros W. Metal organic framework mixed matrix
428 membranes for gas separations. Microporous and Mesoporous Materials 2010; 131: 13-20.

429 45. Elangovan D, Nidoni U, Yuzay I E, Selke SEM and Auras R. Industrial and Engineering
430 Chemistry Research 2011; 50: 11136-42.

List of Tables

Table 1. Thermal characteristics of neat PLLA and PLLA-MIL-53 (Al) MMM films derived from the 2nd heating cycle

Table 2. Thermo-gravimetric analysis of neat PLLA and PLLA-MOF MMM films

Table 3. O_2 permeability coefficient of PLLA and PLLA-20% MIL-53 (Al) MOF MMM films

List of Figures

Figure 1. DSC thermograms of PLLA and PLLA-MIL-53 (Al) MMM films derived from the 2nd heating cycle.

Figure 2a. TGA of PLLA, MIL-53 (Al) and various PLLA-MIL-53 (Al) MMM films.

Figure 2b. First derivative weight change as a function of temperature.

Figure 3a. FTIR Spectra of PLLA and PLLA- MIL-53 (Al) MMM films from wavenumber 3000-2800 cm^{-1}.

Figure 3b. FTIR Spectra of PLLA and PLLA-MIL-53 (Al) MMM films from wavenumber 1650-1850 cm^{-1}.

Figure 3c. FTIR Spectra of PLLA and PLLA-MIL-53 (Al) MMM films from wavenumber 950-800 cm^{-1}.

Figure 4. a). SEM image of MIL-53 (Al), scale size 50 µm b). SEM image of PLLA, scale size 20 µm c). SEM image of PLLA-1% MIL-53 (Al), scale size 20 µm. d). SEM image of PLLA-5% MIL-53 (Al), scale size 20 µm. e). SEM image of PLLA-10% MIL-53 (Al), scale size 20 µm. f). SEM image of PLLA-20% MIL-53 (Al), scale size 20 µm.

Table 1. Thermal characteristics of neat PLLA and PLLA-MIL-53 (Al) MMM films derived from the 2nd heating cycle.

Sample	T_g (ºC)	Cold Crystallization		Melting		
		T_{co} (ºC)	ΔH_c (J/g)	T_m (ºC)	ΔH_m (J/g)	Xc (%)
PLLA	56.6 ± 0. 5 ^{A}	105.1 ± 1.2 ^{A}	8.7 ± 1.9 ^{A}	148.3 ± 0.4 ^{A}	11.7 ± 2.2 ^{A}	3.2 ± 0.1 ^{A}
PLLA-1% MOF	59.0 ± 0.5 ^{B}	108.6 ± 4.2 ^{A}	2.7 ± 2.6 ^{B}	149.0 ± 0.2 $^{A, B}$	4.7 ± 2.8 ^{B}	3.1 ± 0.0 ^{A}
PLLA-5% MOF	57.9 ± 0.3 ^{C}	-	-	149.4 ± 0.4 ^{B}	0.5 ± 0.1 ^{C}	0.5 ± 0.1 ^{B}
PLLA-10% MOF	57.3 ± 1.4 $^{A, B, C}$	-	-	-	-	-
PLLA-20% MOF	60.1 ± 0.6 ^{B}	-	-	-	-	-

Note: Values in the same column with same capital superscript letters are not statistically significantly different at α=0.05. The "-"symbol denotes no results were obtained due to absence of cold crystallization and melting peaks.

459 **Table 2.** Thermo-gravimetric analysis of neat PLLA and PLLA-MOF MMM films.

Sample	Onset Thermal degradation	Weight loss peaks		Peak derivative weight loss
	(ºC)	Peak 1 (ºC)	Peak 2 (ºC)	(%/ºC)
PLLA	341.6 ± 2.0^{A}	136.6 ± 2.0^{A}	376.6 ± 1.4 ^{A}	2.35 ± 0.02 ^{A}
PLLA-1% MOF	330.9 ± 0.8^{B}	136.5 ± 0.9^{A}	359.3 ± 0.8 ^{B}	2.50 ± 0.03 ^{A,B}
PLLA-5% MOF	321.6 ± 1.3^{C}	135.7 ± 0.8^{A}	354.1 ± 0.6 ^{C,D}	2.55 ± 0.06 ^{B}
PLLA-10% MOF	319.6 ± 0.9^{C}	134.6 ± 1.4^{A}	351.2 ± 0.9 ^{D}	2.52 ± 014 ^{A,B}
PLLA-20% MOF	315.2 ± 0.9^{C}	133.3 ± 2.0^{A}	354.5 ± 1.5 ^{C}	2.51 ± 0.01 ^{A,B}

460 *Note*: Values in the same column with same capital superscript letters are not statistically
461 significantly different at α=0.05. The "-"symbol denotes no results were obtained due to absence
462 of cold crystallization and melting peaks.

463

464 **Table 3.** O_2 permeability coefficient of PLLA and PLLA-20% MIL-53 (Al) MOF MMM
465 films.

	O_2 Permeability Coefficient x 10^{-18} (kg.m.m^{-2}.s^{-1}.Pa^{-1})
PLLA	2.27 ± 0.09^{A}
PLLA-20% MOF	2.87 ± 0.34^{B}

466 *Note*: Values in the same column with same capital superscript letters are not statistically
467 significantly different at α = 0.05.

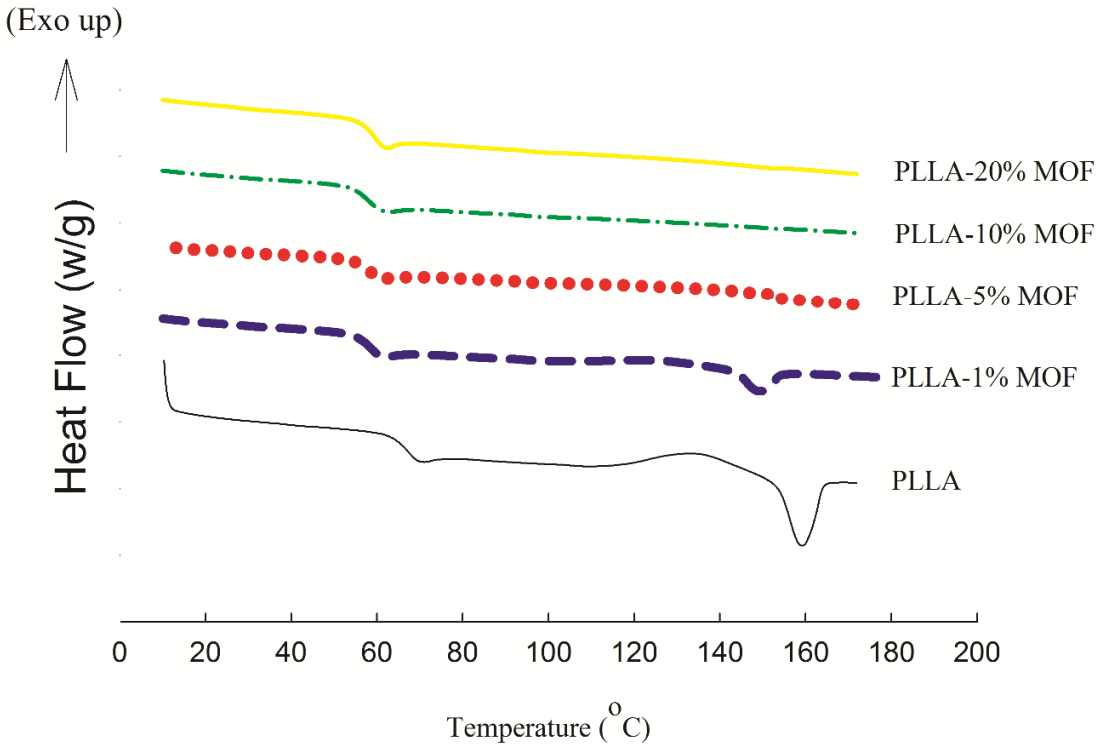

468

469 **Figure 1.** DSC thermograms of PLLA and PLLA-MIL-53 (Al) MMM films derived from
470 the 2nd heating cycle.

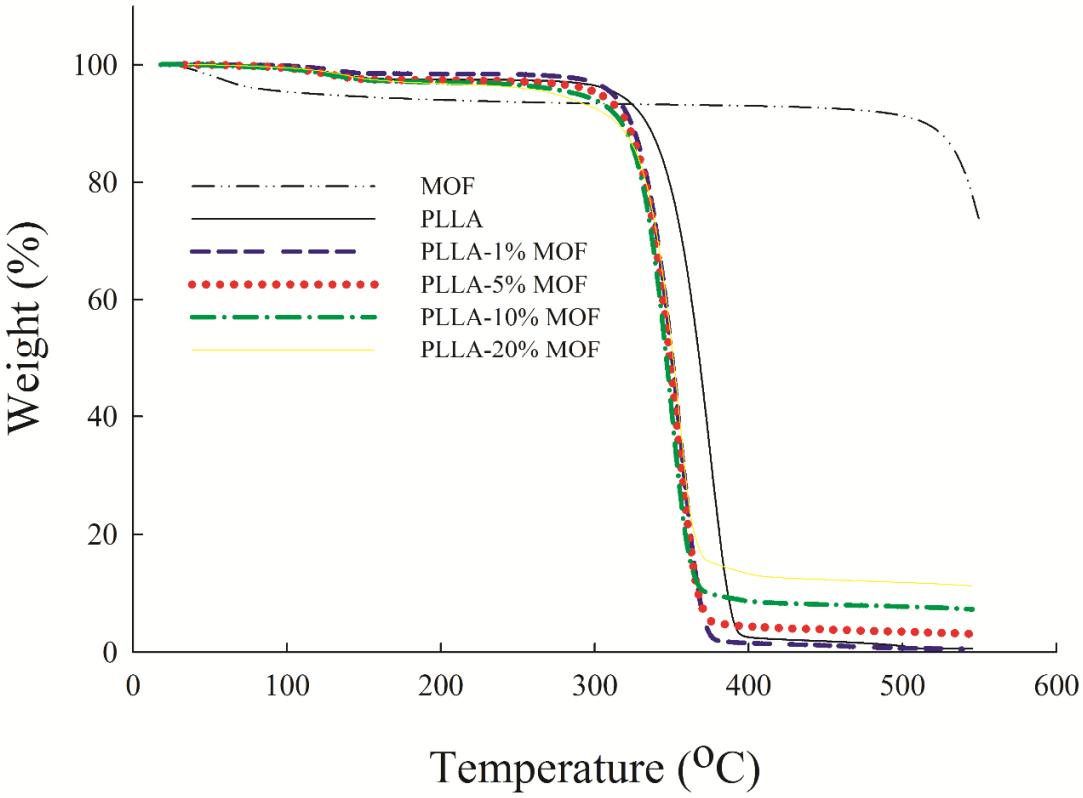

471

472 **Figure 2a.** TGA of PLLA, MIL-53 (Al) and various PLLA-MIL-53 (Al) MMM films.

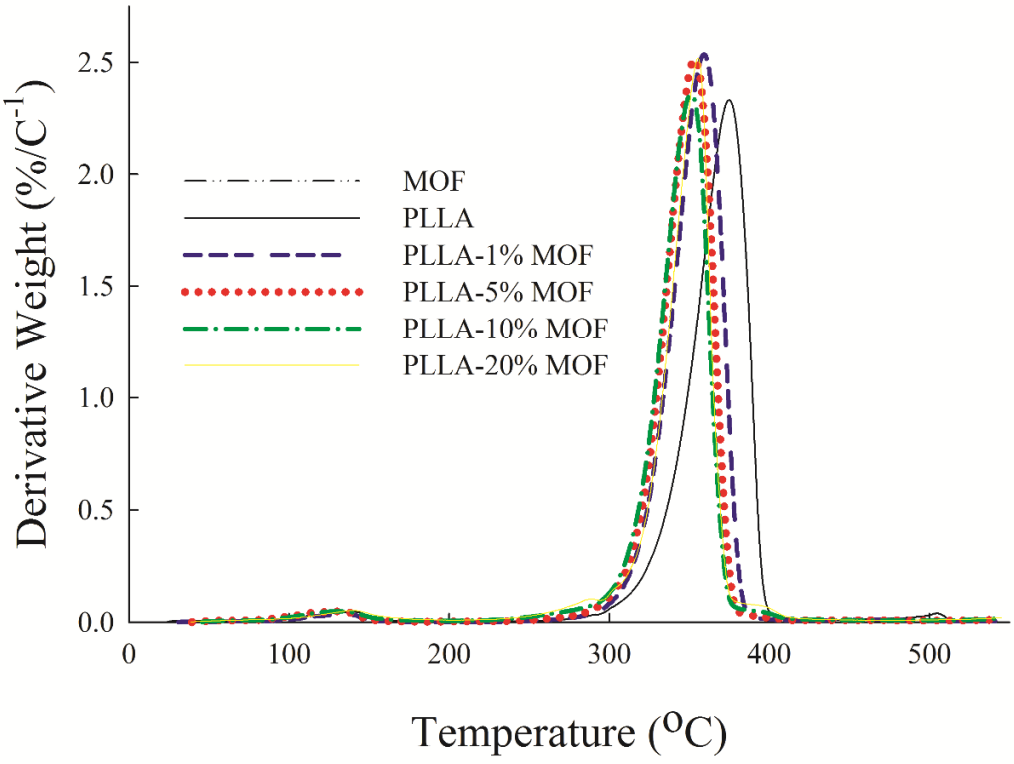

473

474 **Figure 2b.** First derivative weight change as a function of temperature.

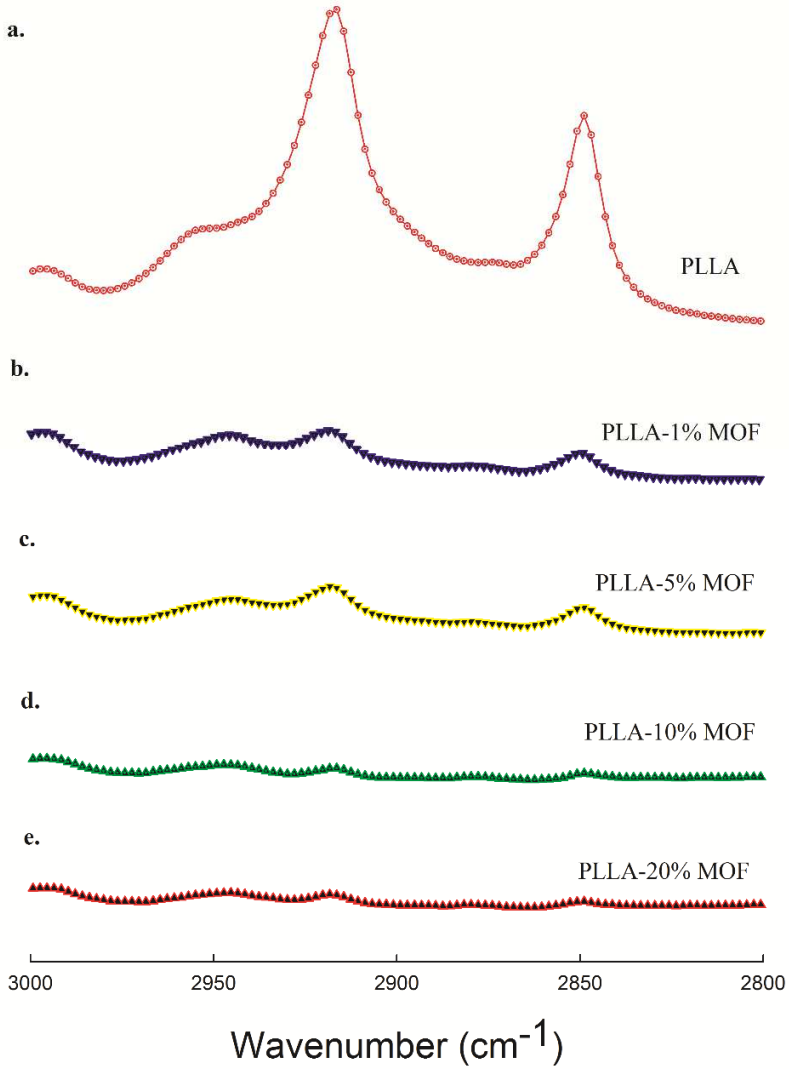

475

476 **Figure 3a.** FTIR Spectra of PLLA and PLLA- MIL-53 (Al) MMM films from wavenumber
477 3000-2800 cm^{-1}.

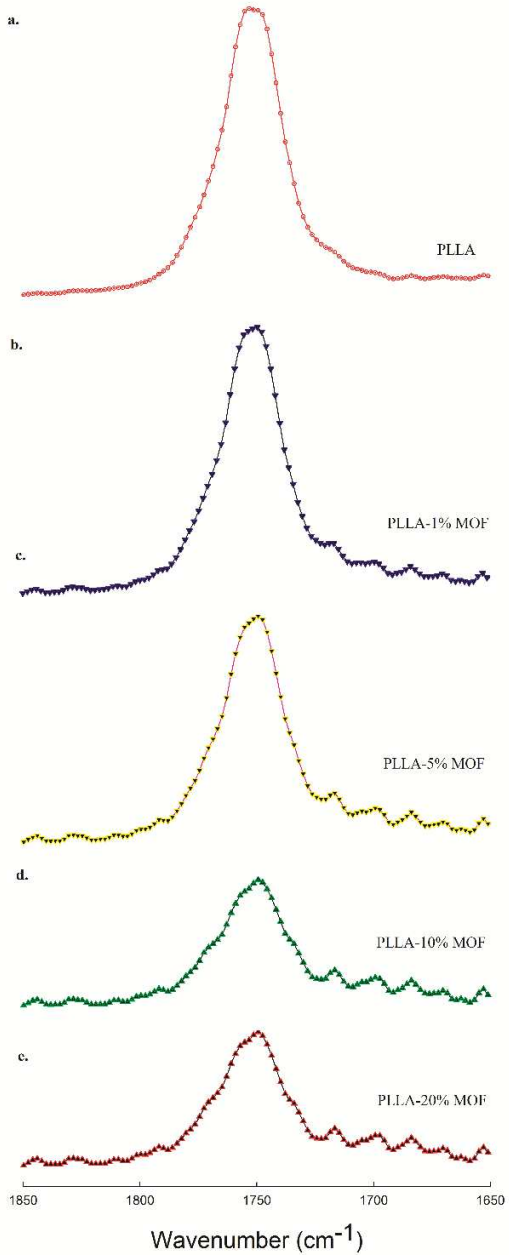

478

479 **Figure 3b.** FTIR Spectra of PLLA and PLLA-MIL-53 (Al) MMM films from wavenumber
480 1650-1850 cm^{-1}.

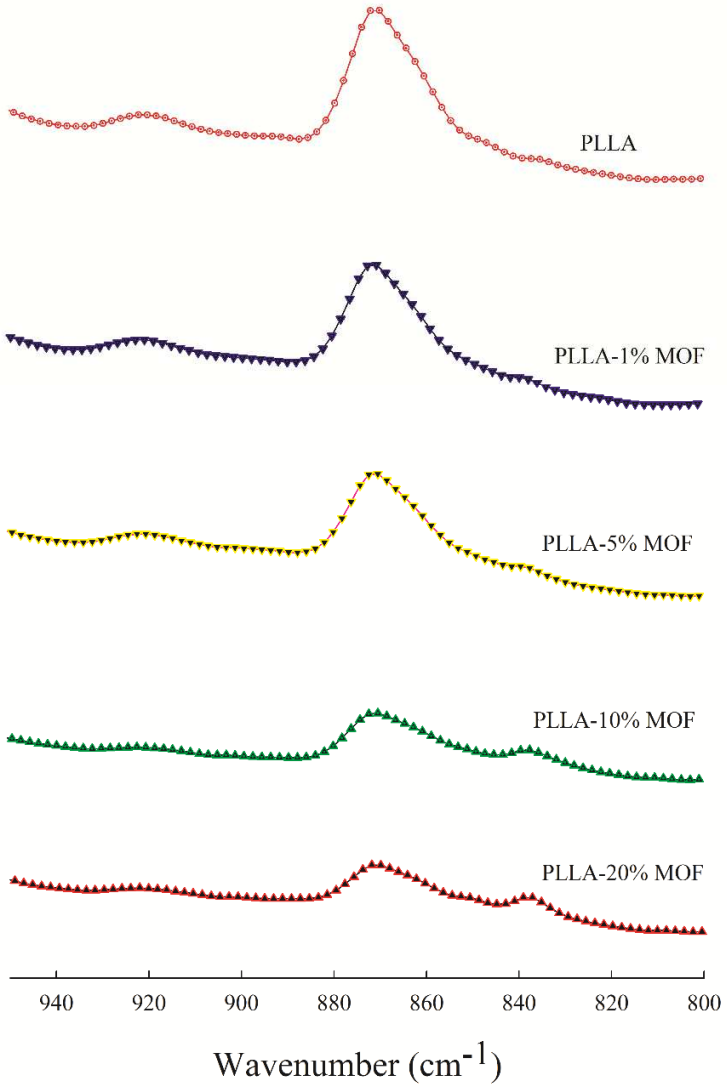

481

482 **Figure 3c.** FTIR Spectra of PLLA and PLLA-MIL-53 (Al) MMM films from wavenumber
483 950-800 cm^{-1}.

484

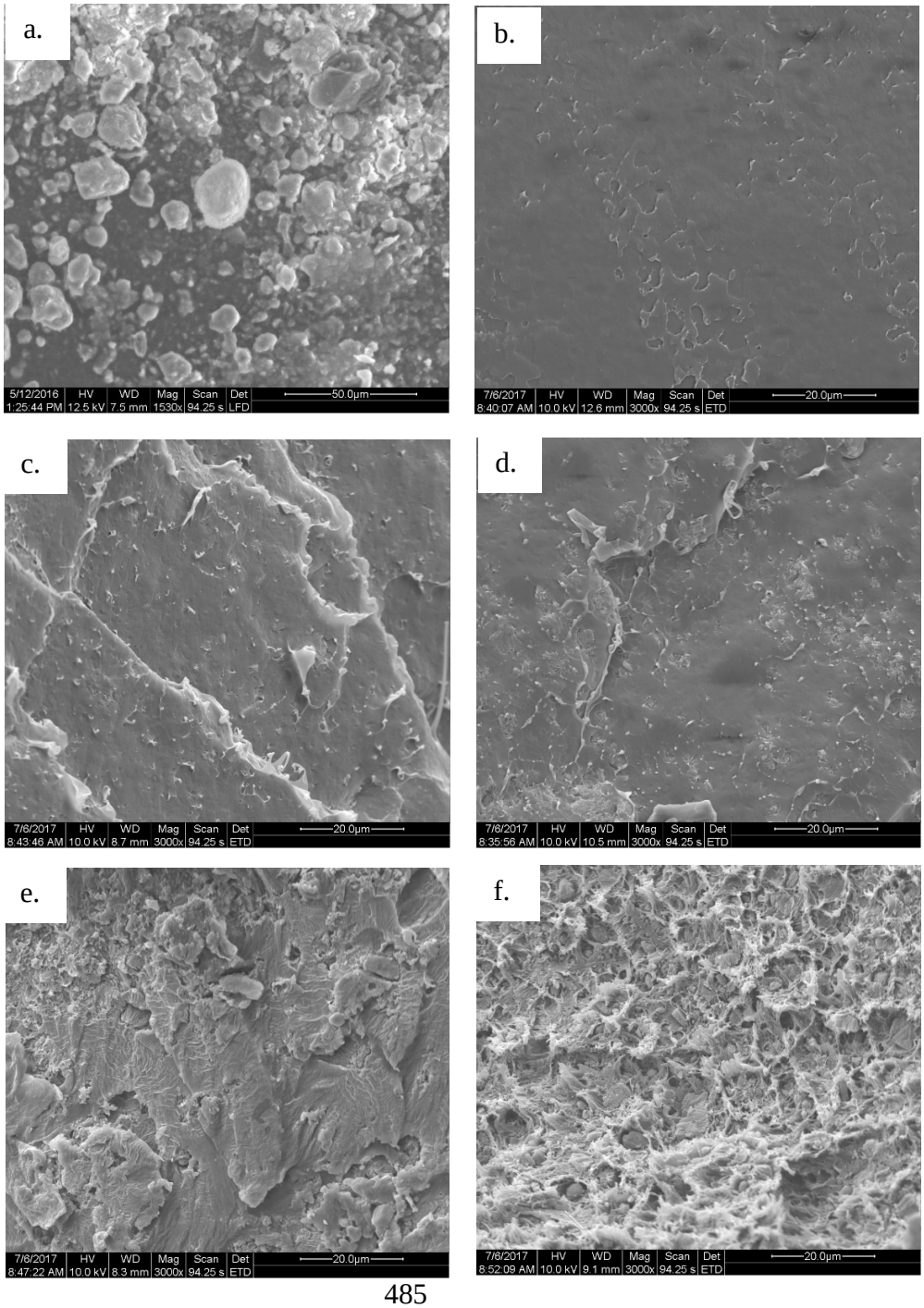

485

486 **Figure 4.** a). SEM image of MIL-53 (Al), scale size 50 µm b). SEM image of PLLA, scale
487 size 20 µm c). SEM image of PLLA-1% MIL-53 (Al), scale size 20 µm. d). SEM image
488 of PLLA-5% MIL-53 (Al), scale size 20 µm. e). SEM image of PLLA-10% MIL-53 (Al),
489 scale size 20 µm. f). SEM image of PLLA-20% MIL-53 (Al), scale size 20 µm.